

# Controlling Ensemble Variance in Diffusion Models: An Application for Reanalyses Downscaling

Fabio Merizzi<sup>1\*</sup>, Davide Evangelista<sup>1</sup> and Harilaos Loukos<sup>2</sup>

<sup>1</sup>Department of Informatics: Science and Engineering (DISI), University of Bologna, Mura Anteo Zamboni 7, Bologna, 40126, Italy .

<sup>2</sup>The Climate Data Factory (TCDF), Paris, France .

\*Corresponding author(s). E-mail(s): [fabio.merizzi@unibo.it](mailto:fabio.merizzi@unibo.it);  
Contributing authors: [davide.evangelista5@unibo.it](mailto:davide.evangelista5@unibo.it);

## Abstract

In recent years, diffusion models have emerged as powerful tools for generating ensemble members in meteorology. In this work, we demonstrate that a Denoising Diffusion Implicit Model (DDIM) can effectively control ensemble variance by varying the number of diffusion steps. Introducing a theoretical framework, we relate diffusion steps to the variance expressed by the reverse diffusion process. Focusing on reanalysis downscaling, we propose an ensemble diffusion model for the full ERA5-to-CERRA domain, generating variance-calibrated ensemble members for wind speed at full spatial and temporal resolution. Our method aligns global mean variance with a reference ensemble dataset and ensures spatial variance is distributed in accordance with observed meteorological variability. Additionally, we address the lack of ensemble information in the CARRA dataset, showcasing the utility of our approach for efficient, high-resolution ensemble generation.

**keywords:** Diffusion Models, Ensemble Generation, Reanalysis Downscaling, Calibrating Variance

## 1 Introduction

Neural approaches to downscaling meteorological reanalyses have proven effective, enhancing spatial and temporal resolutions while reducing computational costs compared to traditional numerical models.

The task is typically framed as an image-to-image prediction, transforming a low-resolution input into a high-resolution output. Widely adopted prediction-based models, such as U-Net [1] and ViT [2], operate deterministically and predict the most likely outcome for a given input. While this can produce high-quality predictions, these models lack the ability to quantify uncertainty or capture extreme events. To address this limitation, conditioned generative approaches, such as diffusion models [3], have gained traction in the scientific community. Unlike deterministic models, diffusion models sample outcomes from a learned distribution, producing diverse ensemble members even when conditioned on the same low-resolution input. These ensembles provide valuable insights into uncertainty estimation, the underlying physical system, and extreme events.

In this paper, we apply a Denoising Diffusion Implicit Model (DDIM) [4] to down-scale meteorological reanalyses, focusing on wind speed. Specifically, we perform the transformation from a global reanalysis (ERA5 [5]) to a regional reanalysis (CERRA [6]) over the European domain. Building on prior work [7], we develop a diffusion model capable of operating across the full CERRA domain and we explore architectural modifications to scale diffusion models to large domains. A critical aspect of generative diffusion is the statistical properties of the generated distribution, particularly the variance. We aim to mathematically analyze how variance relates to the model’s architecture and ensure its spatial distribution aligns with physical expectations. Our analysis begins with a mathematical exploration of the reverse diffusion process, revealing that the variance of ensemble members relates to the number of diffusion steps. We experimentally validate this relationship in the ERA5-to-CERRA task, leveraging the CERRA-EDA [6] ensemble dataset for comparison. Our results demonstrate that adjusting the number of diffusion steps provides sufficient control to match the variance expressed by CERRA-EDA. This establishes our method as a practical tool for tuning ensemble diffusion to align with known uncertainty. Finally, studying the spatial distribution of the variance, we provide a methodology to obtain the optimal number of diffusion steps in specific applications, and we showcase our approach by applying it to a dataset of the Arctic region lacking ensemble information, CARRA [8].

## 1.1 Background

Reanalysis datasets are a cornerstone of modern climate and weather research, providing gridded, high-resolution reconstructions of past atmospheric conditions. Reanalysis are widely used by researchers, institutions, and organizations to support studies ranging from climate variability to extreme event prediction [9–11]. High-resolution reanalyses are often created using downscaling techniques, which refine coarse global climate data into finer spatial and temporal scales. Traditional dynamical downscaling is computationally expensive, requiring significantly more resources than coarser global climate models and leading to data gaps and incomplete assessments of model uncertainty and regional climate variability [12, 13].

In recent years, deep learning has emerged as an effective alternative for downscaling, offering powerful and cost-effective methods for producing high-resolution data [14, 15]. A variety of deep learning models for downscaling have been proposed [16–28],

showcasing their ability to capture complex spatial patterns and generate high-quality outputs across a range of meteorological variables.

Among these methods, diffusion models stand out for their ability to capture the uncertainty of the downscaling process, enabling not only the generation of high-resolution data but also produce probabilistic ensembles by sampling from a latent space. This capability makes them highly effective for modeling uncertainty and variability, which are crucial in meteorological applications [29–35].

Downscaled ensemble datasets are essential for quantifying uncertainties [36–38], detecting extreme events [39], and performing ensemble-based statistical analyses critical for assessing the likelihood of compound extreme events [40, 41]. In recent years an increasing amount of publications focused on the utilization of generative deep learning architectures in the downscaling task, utilizing the inherently probabilistic nature of the models to generate ensemble members.

In [20], the authors extend generative adversarial networks (GANs) to downscale precipitation forecasts, addressing the challenges of adding fine-scale structure and correcting forecast errors. Using high-resolution radar data as ground truth, the study demonstrates that GANs and VAE-GANs can produce spatially coherent precipitation maps while maintaining statistical properties comparable to state-of-the-art post-processing methods. In [32], the authors propose using deep generative diffusion models to emulate and enhance probabilistic weather forecasting. Learning from historical data, diffusion model generate realistic ensemble forecasts at a fraction of the computational cost of traditional physics-based simulations. The generated ensembles replicate the statistical properties and predictive skill of operational forecasts, while also correcting biases, improving reliability, and better capturing probabilities of extreme weather events. This scalable approach has potential applications in both weather forecasting and large-scale climate risk assessment. In [18], the authors propose a statistical downscaling method for satellite sea surface wind (SSW) data using generative adversarial networks (GANs) with a dual learning scheme. The dual learning approach combines high-resolution SSW reconstruction with degradation kernel estimation in a closed loop. In [38], the authors propose a cascading deep learning framework based on generative diffusion models for downscaling tropical cyclone (TC) wind fields from low-resolution ERA5 data ( $0.25^\circ$ ) to high-resolution observations ( $0.05^\circ$ ) at 6-hour intervals. The framework consists of a debiasing neural network to improve wind speed accuracy and a conditional denoising diffusion probabilistic model (DDPM) for super-resolution and ensemble generation. Applied to 85 TC events, the model achieves realistic spatial structures, enabling accurate high-resolution TC wind modeling and risk assessment. In [37], the authors present a hybrid downscaling framework combining dynamical downscaling with generative diffusion models to enhance resolution and improve uncertainty estimates for regional climate projections. The method uses a regional climate model (RCM) to downscale Earth System Model (ESM) outputs to intermediate resolution, followed by a diffusion model for further refinement. Applied to the CMIP6 ensemble, this approach provides more accurate uncertainty bounds, lower errors than bias correction and spatial disaggregation (BCSD), and better captures spectra and multivariate correlations. The

framework offers a cost-effective and accurate alternative for downscaling large climate projection ensembles.

## 1.2 Diffusion models basics

Diffusion models, and in particular Denoising Diffusion Implicit Models (DDIM) [4], are state-of-the-art generative models able to generate highly realistic data from noise. In particular, given a sequence  $\{\alpha_t\}_{t=1}^T \subseteq (0, 1)$  such that  $\alpha_0 \approx 0$  and  $\alpha_T \approx 1$ , called *noise schedule*, a DDIM defines an iterative procedure to turn random noise  $\mathbf{x}_0 \sim \mathcal{N}(\mathbf{0}, \mathbf{I})$  into a new sample  $\mathbf{x}_T \sim p_{gt}(\mathbf{x}_T)$ , where  $p_{gt}(\mathbf{x}_T)$  represents the probability distribution from which the training data is sampled<sup>1</sup>. This procedure is obtained through a simple yet effective idea: let  $\{\mathbf{x}_0, \mathbf{x}_1, \dots, \mathbf{x}_{T-1}, \mathbf{x}_T\}$  be a sequence such that  $\mathbf{x}_0 \sim \mathcal{N}(\mathbf{0}, \mathbf{I})$ ,  $\mathbf{x}_T \sim p_{gt}(\mathbf{x}_T)$ , and  $\mathbf{x}_t \sim p_t(\mathbf{x}_t | \mathbf{x}_T)$  for any  $t = T - 1, \dots, 0$ . If  $p_t(\mathbf{x}_t | \mathbf{x}_T) = \mathcal{N}(\sqrt{\alpha_t} \mathbf{x}_T, (1 - \alpha_t) \mathbf{I})$ , then:

$$\mathbf{x}_t = \sqrt{\alpha_t} \mathbf{x}_T + \sqrt{1 - \alpha_t} \boldsymbol{\epsilon}_t, \quad \boldsymbol{\epsilon}_t \sim \mathcal{N}(\mathbf{0}, \mathbf{I}). \quad (1)$$

Note that the previous equation implies that  $\mathbf{x}_t$  is obtained by interpolating real data  $\mathbf{x}_T$  with random noise  $\boldsymbol{\epsilon}_t$ , with interpolation coefficients  $\sqrt{\alpha_t}$  and  $\sqrt{1 - \alpha_t}$ . Therefore, they are usually referred to as *signal rate* and *noise rate*, respectively. Please refer to section 3.1 for a detailed discussion on how these terms are selected.

Clearly, Equation (1) represents the process that slowly corrupts a true image  $\mathbf{x}_T$  into pure noise  $\mathbf{x}_0$ . To revert this process and generate data from noise, a DDIM considers a neural network  $\boldsymbol{\epsilon}_{\Theta}^t(\mathbf{x}_t)$  trained to extract the noise component  $\boldsymbol{\epsilon}_t$  from  $\mathbf{x}_t$ , i.e.

$$\boldsymbol{\epsilon}_{\Theta}^t(\mathbf{x}_t) \approx \boldsymbol{\epsilon}_t, \quad \forall t = T - 1, \dots, 0. \quad (2)$$

Given that, one can simply invert the process in Equation (1) by sampling  $\mathbf{x}_0 \sim \mathcal{N}(\mathbf{0}, \mathbf{I})$  and then iteratively updating:

$$\mathbf{x}_t = \sqrt{\frac{\alpha_t}{\alpha_{t-1}}} \mathbf{x}_{t-1} + \left( \sqrt{1 - \alpha_t} - \sqrt{\frac{\alpha_t(1 - \alpha_{t-1})}{\alpha_{t-1}}} \right) \boldsymbol{\epsilon}_{\Theta}^{t-1}(\mathbf{x}_{t-1}). \quad (3)$$

After  $T$  steps, this process leads to a new sample  $\mathbf{x}_T \sim p_{gt}(\mathbf{x}_T)$ . For a detailed introduction to DDIM, please refer to [4, 42, 43].

A property of DDIM that is crucial for our work is the possibility of *skipping* a few steps in the generative process. This is achieved by setting a *step-size*  $\Delta t \in \mathbb{N}$  and modifying Equation (3) as:

$$\mathbf{x}_t = \sqrt{\frac{\alpha_t}{\alpha_{t-\Delta t}}} \mathbf{x}_{t-\Delta t} + \left( \sqrt{1 - \alpha_t} - \sqrt{\frac{\alpha_t(1 - \alpha_{t-\Delta t})}{\alpha_{t-\Delta t}}} \right) \boldsymbol{\epsilon}_{\Theta}^{t-\Delta t}(\mathbf{x}_{t-\Delta t}). \quad (4)$$

---

<sup>1</sup>Note that here we use a slightly different notation compared to e.g. [4], as we consider the time running *reversely*. We made this choice as this notation simplifies the mathematical derivation of our formula in section 3.1.

Note that the choice  $\Delta t = 1$  recovers the original generative process, while  $\Delta t > 1$  allows for a faster generation, possibly at the expense of quality. This modification can be relevant when the neural network model  $\epsilon_{\Theta}^t(\mathbf{x}_t)$  is particularly large, or when the dimensionality of the data  $\mathbf{x}_T$  is big. Indeed, when this happens, computing  $\epsilon_{\Theta}^{t-\Delta t}(\mathbf{x}_{t-\Delta t})$  could be time-prohibitive, and reducing the amount of time this operation has to be done to reach the end of the process is crucial for its applicability. Since the number of iterations of Equation (4) equals to  $N = \frac{T}{\Delta t}$ , increasing  $\Delta t$  leads to a faster generation process.

In this work we argue that the importance of the selection of the step-size  $\Delta t$  is not limited to the time-efficiency of the generative process, but it can also be used to control the variance of the sampled data: a key aspect when these models are employed for generating ensembles.

### 1.3 Notations

Throughout this article, we will make use of some notations, which we report here for completeness. In particular, we use lower-case non-bold latin characters to indicate scalar values, lower-case bold latin characters to indicate vectors, and upper-case bold latin characters to indicate matrices. Moreover, we will denote as  $\mathbf{0}$ ,  $\mathbf{1}$  the vector of all zeros and all ones, respectively, and as  $\mathbf{I}$  the identity matrix. If  $\mathbf{x}$  and  $\mathbf{y}$  are two vectors with the same dimension, then  $\mathbf{x} \geq \mathbf{y}$  means that  $x_i \geq y_i$  for every  $i$ . The data is therefore assumed to be a vector of dimension  $n$ , which corresponds to the flattened version of the  $(S \times M \times h \times w)$ -dimensional array if it is indicated with a lowercase bold letter, while it is treated as a tensor if indicated with an uppercase bold letter. For example, if  $\mathbf{X} \in \mathbb{R}^{S \times M \times h \times w}$  represents the usual tensor-shaped dataset with  $S$  datapoints,  $M$  channels, and spatial dimension  $h \times w$ , then  $\mathbf{x} \in \mathbb{R}^n$  represents its flattened version, with  $n = S \cdot M \cdot h \cdot w$ .

### 1.4 Structure of the article

The remainder of this paper is organized as follows. In Section 2 we introduce the datasets employed for the experiments, namely CERRA, CERRA-EDA and CARRA, representing a high-resolution world map with positional information of the wind. In Section 3 we provide the theoretical background for the proposed idea, and show a possible interpretation of the observed phenomena. Next we introduce the methodology applied in the successive experiments, described in Section 5. Finally, in Section 6 we conclude the paper by summarizing our results.

## 2 Data

In this section we describe the primary datasets used in this study. Our task involves using the global reanalyses ERA5 [44] as the low-resolution input to condition our model in predicting a high-resolution downscaled counterpart, trained on the regional reanalyses CERRA [6]. The resulting ensemble members are validated against CERRA-EDA, an ensemble version of CERRA at half the temporal and spatial resolution. We will also apply our methods to CARRA, a dataset built on the same core

model as CERRA and that covers the Arctic region, but lack ensemble members. This section begins with a brief introduction to ERA5, followed by a focused discussion on CERRA, CARRA, and CERRA-EDA.

## 2.1 ERA5

ERA5 [5], the fifth generation ECMWF reanalysis, is a globally recognized dataset extensively utilized in climate and atmospheric research. Spanning from 1940 to the present, it provides hourly estimates of atmospheric, land, and oceanic variables at a  $0.25^\circ$  horizontal resolution (approximately 30 km) and 137 vertical levels. Based on the ECMWF Integrated Forecasting System, ERA5 incorporates advanced numerical weather prediction models and satellite data, ensuring high reliability and precision [44]. Its widespread use spans diverse applications, including precipitation trends, temperature analysis, wind studies, and extreme event research, making it an indispensable resource in climate science.

## 2.2 CERRA

The Copernicus Regional Reanalysis for Europe (CERRA [6]) is a sophisticated high-resolution Regional ReAnalysis (RRA) dataset specifically designed for the European region. It is a product of the European Copernicus Climate Change Service (C3S), executed through a contract with the Swedish Meteorological and Hydrological Institute (SMHI), in collaboration with subcontractors Meteo-France and the Norwegian Meteorological Institute. CERRA operates at a high 5.5 km horizontal resolution, offering enhanced spatial detail for meteorological variables across Europe.

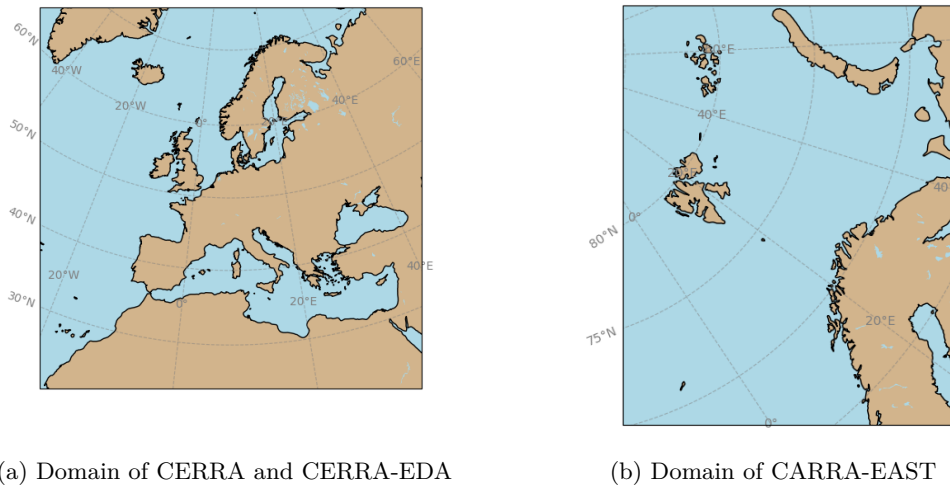


**Fig. 1:** Comparison of CERRA and CARRA-EAST domains.

To achieve this fine resolution, CERRA relies on the global ERA5 reanalysis for initial and boundary conditions. In addition to ERA5, CERRA incorporates an extensive array of high-resolution observational data, covering conventional and satellite sources, along with physiographic datasets that represent surface characteristics. One innovative aspect of CERRA is its integration with the CERRA-EDA (Ensemble of Data Assimilation), which is a 10-member ensemble system that provides essential background error statistics. These statistics, recalculated every second day, enable CERRA to dynamically adjust initial conditions, significantly enhancing the accuracy of data assimilation and model outputs.

CERRA provides a comprehensive range of meteorological variables, including temperature, humidity, wind speed and direction, precipitation, and cloud cover, all presented on a consistent  $1069 \times 1069$  grid. Unlike ERA5’s hourly structure, CERRA’s temporal resolution combines reanalysis and forecast data, featuring eight reanalysis time points daily at three-hour intervals starting from 00 UTC. Each reanalysis cycle is followed by a six-hour forecast period, with additional 30-hour forecasts generated at 00 UTC and 12 UTC. For this study, we focus exclusively on the reanalysis data. CERRA employs a Lambert Conformal Conic (LCC) projection to minimize distortion at high latitudes, ensuring greater accuracy in polar regions.

### 2.3 CARRA

The C3S Arctic Regional Reanalysis (CARRA) dataset [8] addresses the unique environmental and climatic conditions of the Arctic region, which are insufficiently captured by global reanalyses such as ERA5. While ERA5 provides a 31 km global resolution, CARRA offers 2.5 km horizontal resolution, capturing finer details essential for understanding the Arctic’s rapidly changing climate. Observational records and climate projections show that warming in the Arctic occurs at over twice the global average rate, leading to increased environmental and economic activities and driving a need for detailed data to support climate adaptation and management in the region.

CARRA leverages the same HARMONIE-AROME weather prediction model as CERRA, enhanced for reanalysis applications at the ECMWF high-performance computing facility. It features a three-hourly analysis update with a comprehensive three-dimensional variational data assimilation scheme, incorporating diverse data sources. This includes an extensive array of local observations from Nordic countries and Greenland, advanced satellite-derived glacier albedo data, improved sea ice and snow initialization, and high-resolution physiography and orography data, specifically adjusted for the Arctic’s unique topography.

The dataset spans two key domains:

- CARRA-West, covering Greenland, the Labrador Sea, Davis Strait, Baffin Bay, Denmark Strait, Iceland, Jan Mayen, the Greenland Sea, and Svalbard.
- CARRA-East, which includes Svalbard, Jan Mayen, Franz Josef Land, Novaya Zemlya, Barents Sea, and the northern regions of the Norwegian Sea and Scandinavia.

These domains encompass the Arctic’s four largest land ice bodies, including the Greenland Ice Sheet and the Austfonna Ice Cap, which are focal points in climate research. CARRA’s high resolution allows for accurate representation of critical

Arctic-specific weather phenomena, such as polar lows in the North Atlantic and Greenland’s downslope katabatic winds, which have significant implications for local communities and maritime activities.

The CARRA reanalysis is driven by ERA5 global reanalysis data for boundary conditions, integrating enhanced observations and ArcticDEM-based elevation data. CARRA also provides critical improvements in data quality through the assimilation of satellite observations (e.g., radiances, scatterometer data) and refined upper-air data algorithms, making it a powerful tool for Arctic climate monitoring. Covering the period from September 1990 to the present, CARRA supports comprehensive climate analysis with monthly updates that maintain a 2-3 month latency, ensuring the dataset remains relevant and accurate for ongoing climate research and operational needs.

For our works we will focus on the CARRA-EAST domain.

## 2.4 CERRA-EDA

CERRA-EDA [45] is an Ensemble of Data Assimilation (EDA) system comprising 10 members. It is based on the same code as the deterministic CERRA system and uses the same observational data, with the exception of the Microwave Sounding Unit and has a lower 11-km horizontal resolution.

Each ensemble member in CERRA-EDA is generated by perturbing observations prior to data assimilation. One control member is initialized without any perturbations, while the other nine members incorporate Gaussian-distributed random perturbations within the estimated observational errors. No perturbations are applied to Sea Surface Temperature (SST), sea ice, or physical parameters. The lateral boundary conditions for CERRA-EDA are provided by the ERA5 ensemble, which includes 10 members and operates with a 63-km horizontal grid.

The analyses generated by CERRA-EDA are used to produce six-hour forecasts, from which background error covariances are estimated. CERRA relies on CERRA-EDA’s output, which supplies essential background error statistics and is integral to the data assimilation process.

CERRA-EDA is run in advance of the deterministic system, though this typically does not hinder production due to CERRA-EDA’s faster processing enabled by its lower resolution and longer time steps, with the 10 ensemble members operating in parallel.

## 3 Methodology

In this section we quickly review our signal and noise scheduling methodology before delving into the mathematical reasoning behind the control of variance via the number of diffusion steps. In particular, we derive an explicit formula to predict the variance of the generated data, which shows how it depends on the number of diffusion steps.

### 3.1 Signal and noise rates

In Section 1 we discussed the importance of the diffusion schedule  $\{\alpha_t\}_{t=1,\dots,T}$  in the generation process of DDIM. Recently, various schedules have been proposed to



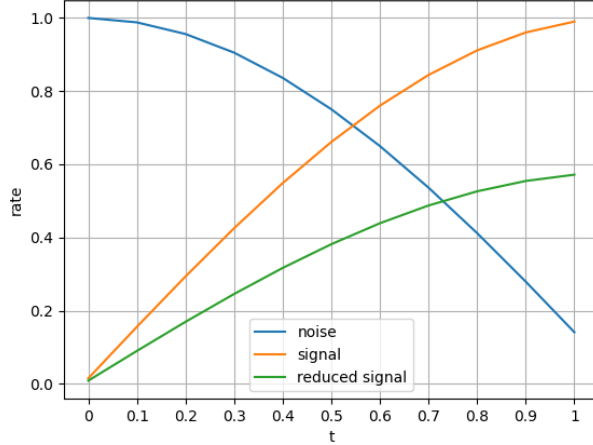


**Fig. 2:** Reverse diffusion signal and noise ratios with cosine scheduling, including the reduced signal rate

find a perfect balance between the signal and noise in the diffusion process, including linear schedules [3] and sinusoidal schedules [4, 46]. In this study, we adopt sinusoidal functions due to their ability to achieve smooth and controlled transitions between signal and noise components, which is crucial for effective denoising and high-quality image generation. In particular, we consider the following choice for the signal rate as in [42]:

$$\sqrt{\alpha_t} = \sin\left(\pi \frac{T-t}{T}\right). \quad (5)$$

Therefore, the noise rate becomes:

$$\sqrt{1 - \alpha_t} = \cos\left(\pi \frac{T-t}{T}\right), \quad (6)$$

for which it holds that  $(\sqrt{\alpha_t})^2 + (\sqrt{1 - \alpha_t})^2 = \sin^2\left(\pi \frac{T-t}{T}\right) + \cos^2\left(\pi \frac{T-t}{T}\right) = 1$ , ensuring that the noisy images, formed as a weighted sum of signal and noise, consistently maintain unit variance [46, 47]. The extremes of the schedule (i.e. when  $t = 0$  and  $t = T$ ) can be problematic, as near-pure signal or noise levels often cause instability. Following common practice [47, 48], we clamp the extremes to maintain a balanced Signal-to-Noise Ratio (SNR), preventing degenerate cases and ensuring stable training and reliable reverse diffusion.

As for the time discretization, we consider a uniform subdivision of the  $[0, T]$  range into  $T$  intervals, so that  $t \in \{0, 1, \dots, T\}$ . Note that, when a step-size  $\Delta t > 1$  is considered, then clearly the time-domain becomes:

$$t \in \{0, \Delta t, 2\Delta t, \dots, N\Delta t\}, \quad (7)$$

where  $N = \frac{T}{\Delta t}$  represents the number of timesteps of our generative process.

### 3.2 Controlling the variance

The generative process for DDIM involves a sequence of denoising operations alternated with the re-injection of the same noise. Our findings reveal that the key aspect of controlling the variance is selecting the number of diffusion steps. In this section, we analyze the evolution of the variance through the iterative diffusion process and we provide an intuition on how the number of diffusion steps  $N$  influences the variance of the generated data. We remark that the diffusion process in DDIM is defined by sampling  $\mathbf{x}_0 \sim \mathcal{N}(\mathbf{0}, \mathbf{I})$  and then iterating through:

$$\mathbf{x}_t = \sqrt{\frac{\alpha_t}{\alpha_{t-\Delta t}}} \mathbf{x}_{t-\Delta t} + c_{t-\Delta t} \epsilon_{\Theta}^{t-\Delta t}(\mathbf{x}_{t-\Delta t}), \quad (8)$$

where we defined  $c_{t-\Delta t}$  as:

$$c_{t-\Delta t} := \sqrt{1 - \alpha_t} - \sqrt{\frac{\alpha_t(1 - \alpha_{t-\Delta t})}{\alpha_{t-\Delta t}}}, \quad (9)$$

to simplify the notation. We also recall that the diffusion schedule  $\{\alpha_t\}_{t=0, \dots, T}$  is selected such that  $\alpha_0 \approx 1$  and  $\alpha_T \approx 0$ . Note that  $\alpha_T \neq 0$  as we clamped its value to avoid instabilities during training, as we already discussed in section 3.1.

Let  $\mathbf{x}_0$  be an  $n$ -dimensional random variable with Gaussian distribution such that  $\mathbb{E}[\mathbf{x}_0] = \mathbf{0}$  and  $\text{Var}(\mathbf{x}_0) = \mathbf{I}$ , and let  $\{\mathbf{x}_t\}_{t=0, \dots, T}$  be the stochastic process defined in (8). Since the full variance matrix  $\text{Var}(\mathbf{x}_t)$  has dimension  $n \times n$ , which is prohibitive from a computational point of view, in this work we limit our analysis to the element-wise variance, defined as:

$$\mathbf{v}(\mathbf{x}_t)_i := \text{Var}(\mathbf{x}_t)_{i,i}, \quad (10)$$

which is a vector of dimension  $n$ , representing the variance between each pixel of  $\mathbf{x}_t$  with itself, ignoring the relationship with the adjacent pixels. Note that this choice is coherent with our task, as we want to study the pixel-wise uncertainty of DDIM downscaling, and taking into consideration the correlation between adjacent pixels is beyond the scope of this analysis.

It is not difficult to show (see Appendix A) that the element-wise variance has similar properties to the classical variance, and in particular:

- (P1)  $\mathbf{v}(a\mathbf{x}_t) = a^2\mathbf{v}(\mathbf{x}_t)$ ,
- (P2)  $\mathbf{v}(\mathbf{x}_t + \mathbf{y}_t) = \mathbf{v}(\mathbf{x}_t) + \mathbf{v}(\mathbf{y}_t) + 2\mathbf{v}(\mathbf{x}_t, \mathbf{y}_t)$ ,

where  $\mathbf{v}(\mathbf{x}_t, \mathbf{y}_t)$  is the element-wise covariance between  $\mathbf{x}_t$  and  $\mathbf{y}_t$ .

**Proposition 3.1.** Let  $\mathbf{m}_t := \mathbb{E}[\mathbf{x}_t]$  and  $\mathbf{v}_t := \mathbf{v}(\mathbf{x}_t)$ . Then, for any  $t = \Delta t, \dots, N\Delta t$ , it holds:

$$\mathbf{v}_t \approx \mathbf{F}_t \mathbf{v}_{t-\Delta t} + \mathbf{g}_t, \quad (11)$$

where:

$$\begin{aligned} \mathbf{F}_t &:= \frac{\alpha_t}{\alpha_{t-\Delta t}} \mathbf{I} + \mathbf{J}_t, \\ \mathbf{J}_t &:= 2\sqrt{\frac{\alpha_t}{\alpha_{t-\Delta t}}} c_{t-\Delta t} \text{diag} \left( \nabla_{\mathbf{m}_{t-\Delta t}} \epsilon_{\Theta}^{t-\Delta t}(\mathbf{m}_{t-\Delta t}) \right), \\ \mathbf{g}_t &:= c_{t-\Delta t}^2 \mathbf{1}. \end{aligned}$$

*Proof.* See Appendix A. □

Note that (11) represents a first-order linear recurrence equation of dimension  $n$  with non-constant coefficients, for which there exists a closed formula that can be used to compute  $\mathbf{v}_T$ , the variance of the generated data, as summarized in the following Theorem.

**Theorem 3.2.** Let  $\mathbf{F}_t$ ,  $\mathbf{J}_t$ , and  $\mathbf{g}_t$  defined as in Proposition 3.1, and let  $\Delta t$  be a fixed step-size for DDIM, so that any timestep  $t$  can be written as  $i\Delta t$  for  $i = 0, \dots, N$ . Note that  $\mathbf{v}_0 = \mathbf{1}$ , the vector of all ones, as  $\mathbf{x}_0 \sim \mathcal{N}(\mathbf{0}, \mathbf{I})$ . Then, defining  $\mathbf{F}_{(N+1)\Delta t}$  to be the identity matrix to simplify the notation, it holds:

$$\mathbf{v}_T \approx \left( \prod_{i=1}^N \mathbf{F}_{i\Delta t} \right) \mathbf{1} + \sum_{i=1}^N \left[ \left( \prod_{k=i+1}^{N+1} \mathbf{F}_{k\Delta t} \right) \mathbf{g}_{i\Delta t} \right]. \quad (12)$$

*Proof.* See Appendix A. □

Notably, Theorem 3.2 not only allows for the explicit computation of the element-wise variance of  $\mathbf{x}_T$ , but it also underlines the dependence of  $\mathbf{v}_T$  on the number of diffusion timesteps. Indeed, if, for example, both  $\mathbf{F}_{i\Delta t} \geq \mathbf{0}$  and  $\mathbf{g}_{i\Delta t} \geq \mathbf{0}$ , then Equation (12) clearly implies that  $\mathbf{v}_T$  monotonically grows as a function of  $N$ . Specifically, increasing the step size  $\Delta t$  (and consequently reducing the number of timesteps  $N$ ) results in fewer terms being included in the summation that computes  $\mathbf{v}_T$ , thereby decreasing its value.

## 4 Experimental Setting

In this section, we describe the pre-processing, training, and evaluation strategies required to adapt the diffusion model for high-resolution downscaling across the full CERRA domain. The transition to larger spatial scales necessitated adjustments to both data handling and model architecture to ensure consistent performance. We focus on data selection and pre-processing in Section 4.1, followed by a detailed explanation of the modifications required for training on the full domain in Section 4.2.

## 4.1 Data selection and pre-processing

The diffusion model performs downscaling in an image-to-image manner, transforming low-resolution ERA5 data into high-resolution CERRA or CARRA outputs while maintaining alignment over the same spatial domain for input and output. The primary experimental framework of our study focuses on downscaling wind speed from ERA5 to CERRA over the full CERRA domain and comparing the ensemble results with the CERRA-EDA dataset. Our model will be trained solely on the CERRA data and no input of CERRA-EDA is used during training, ensuring that the model will learn the ensemble variability only from the CERRA data itself.

The CERRA domain spans a grid of  $1069 \times 1069$  points across Europe, represented in a Lambert Conformal Conic (LCC) projection. The complete CERRA dataset covers the period from September 1984 to June 2021; for our experiments, we utilized data from 1985 to 2010 for training and from 2016 for ensemble testing. Additionally, we evaluated overall performance for the entire decade from 2011 to 2020, though computational constraints limited ensemble variance testing to the year 2016. In our diffusion model, ERA5 data serves as the conditioning input, re-gridded to align with CERRA’s LCC grid. Wind speed,  $s$ , is derived from the two wind components,  $s_u$  and  $s_v$ , as:

$$s := \left\| \begin{bmatrix} s_u \\ s_v \end{bmatrix} \right\|_2 = \sqrt{s_u^2 + s_v^2}$$

Our diffusion model is based on a residual convolutional denoiser, which benefits from input dimensions divisible by two at multiple levels. To ensure consistency between the downsample and upsample paths, we augment the original grid size ( $1069 \times 1069$ ) with mirroring padding, resulting in a final input size of  $1072 \times 1072$ . Our conditioning is implemented via concatenation on the input of the denoising network, to equalize the dimension we opt to upscale the ERA5 data to  $1069 \times 1069$  via bilinear interpolation, and then we apply the same mirroring padding to ensure spatial consistency.

To compare our diffusion-based ensembles with the existing CERRA-EDA ensemble members, we note that CERRA-EDA operates at half the spatial resolution of CERRA ( $565 \times 565$ ) and a temporal resolution of six hours, also halved relative to CERRA. For consistency, we train our model exclusively on full-resolution CERRA data with a three-hour temporal resolution. Wind speed is an instantaneous value, therefore six-hourly outputs can be generated using conditioning information at the same temporal resolution. The generated outputs retain the full CERRA resolution; for comparison with CERRA-EDA, we apply bilinear interpolation to downscale the results.

Diffusion models require standardized inputs to balance signal and noise rates effectively. We apply a standardizer that normalizes inputs using the mean and variance computed across the training set, ensuring consistent scaling across batches. It is important to note that this variance is relative to the training data and is distinct from the ensemble variance between members produced by the diffusion model.

This normalization is applied to both high-resolution images (signal rates) and low-resolution conditioning data, aligning their scales and simplifying the learning task. Experimentally, this approach demonstrated improved performance and stability.

## 4.2 Training on the full domain

The general structure of our diffusion model follows the framework established in [7]. The model utilizes a residual U-Net [1, 49] as a denoiser. Training is conducted by uniformly sampling signal-to-noise ratios from the sinusoidal noise scheduling functions, optimizing the mean absolute error (MAE) between the sampled noise and the predicted noise.

Scaling the diffusion model to the full CERRA domain, with image sizes of  $1069 \times 1069$ , required modifications to a model originally designed for downscaling images up to  $256 \times 256$ . These adaptations involved adjustments to both the noise schedule and the network architecture to ensure effective performance at higher resolutions.

Recent findings [47, 48] have demonstrated that cosine noise schedules can reduce the effective noise added by the model as image size increases. This occurs because redundancy in data, such as correlations among nearby pixels, typically increases with resolution, and the independently added noise becomes easier to denoise in larger images. Consequently, noise schedules optimized for smaller resolutions may not perform as effectively at higher resolutions. To address this issue, we introduce a constant scaling factor  $\lambda > 1$  to reduce the signal rate in the noise schedule. For an input  $\mathbf{x}_T \sim p_{gt}(\mathbf{x}_T)$  and a scaling factor  $\lambda$ , the noise schedule eq. (1) is modified as follows:

$$\mathbf{x}_t = \sqrt{\alpha_t} \frac{\mathbf{x}_T}{\lambda} + \sqrt{1 - \alpha_t} \boldsymbol{\epsilon}_t \quad (13)$$

Experimentally, setting the value  $\lambda = 3$  improved training efficiency and overall model performance, which is a crucial aspect for large-scale ensemble diffusion applications. A comparison of signal and noise ratios with the scaled signal rate is shown in Figure 2. Notably, applying the same scaling to the low-resolution conditioning signal further stabilized the training process.

While the core U-Net architecture remained largely unchanged, scaling to larger domains required increasing the number of residual blocks in the bottleneck. This adjustment improved performance when generating larger images [48]. The model’s performance across the increased domain remained comparable to that observed at smaller resolutions, with the bottleneck modification enhancing its ability to process higher-resolution inputs effectively.

The diffusion model is trained on the ERA5 to CERRA task for wind speed on the full domain, utilizing data from 1985 to 2010 for training. The training is run on three A100 GPUs, utilizing the AdamW optimizer.

## 5 Experiments

Our primary experimental objective is to evaluate the behavior of ensemble variance while changing the timestep  $\Delta t$ . While a comprehensive analysis of the ensemble diffusion model’s performance across the entire CERRA domain is beyond the scope of this paper, we ensure that the model operates within a realm of satisfactory performance. To achieve this, we begin—similar to [7]—by comparing our model’s performance against bilinearly interpolated ERA5 data and a residual U-Net model trained for the same task. The results, obtained by computing the Mean Squared Error (MSE) and SSIM between the high-resolution output produced by the model and the original CERRA, are shown in Table 1.

	Bilinear	U-Net	DDIM (Our)
MSE ( $\downarrow$ )	3.73e-03	2.50e-04	2.54e-04
SSIM ( $\uparrow$ )	0.751	0.892	0.923

**Table 1:** Performance of ensemble diffusion against bilinear interpolation and U-Net for the years 2011-2020.

Testing for the years 2011–2020, the ensemble diffusion model achieves an MSE of  $2.54 \cdot 10^{-4}$ , compared to  $2.50 \cdot 10^{-4}$  for the U-Net and  $3.73 \cdot 10^{-3}$  for bilinear interpolation. For SSIM, bilinear interpolation scores 0.751, the U-Net scores 0.892, and ensemble diffusion achieves the highest score of 0.923. Ensemble diffusion was executed with  $N = 2$  diffusion steps and an ensemble of 10 members.

These results confirm that the diffusion model delivers satisfactory performance, with MSE values approximately an order of magnitude better than bilinear interpolation and comparable to those of the U-Net. Additionally, as expected, the diffusion model outperforms both alternatives in terms of SSIM. The proposed metrics were calculated on normalized data.

### 5.1 Quantifying variance

The first aspect of variance analysis we evaluate in our experiments is understanding how the model’s expressed variance changes with the number of diffusion steps, as detailed in Section 3.2. For this experiment we selected the year 2016 and computed the ensemble variance for 10 members for all the year at 6h intervals, matching the existing format of the CERRA-EDA ensemble. Furthermore, we used bilinear interpolation to reduce the spatial dimension of our output image from  $1069 \times 1069$  to  $565 \times 565$ , also matching the existing CERRA-EDA format. Having obtained a comparable dataset, we proceeded to calculate the pixel-wise variance for the ensemble member of each ensemble of the year, finally calculating the mean variance, a value representing the overall variance expressed by the diffusion model.

Given a dataset of ensembles  $\mathbf{D} \in \mathbb{R}^{S \times M \times h \times w}$ , where  $S$  represents the number of samples for 2016,  $M = 10$  is the number of ensemble members for each datapoint, and

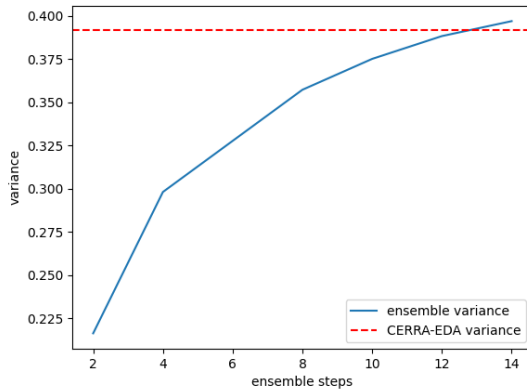


**Fig. 3:** Plotting the global mean variance  $\mu_V$  of ensemble diffusion for different number of steps against CERRA-EDA

$(h, w) = (565, 565)$  are the spatial dimensions, we compute the pixel-wise variance across the ensemble members  $\mathbf{V} \in \mathbb{R}^{S \times M \times 565 \times 565}$ , such that for each sample  $i = 1, \dots, S$ , and any spatial coordinate  $(x, y) \in \{1, \dots, h\} \times \{1, \dots, w\}$ ,

$$\mathbf{V}_i(x, y) = \frac{1}{M} \sum_{j=1}^M \left( \mathbf{D}_{i,j}(x, y) - \frac{1}{M} \sum_{k=1}^M \mathbf{D}_{i,k}(x, y) \right)^2. \quad (14)$$

We then compute the mean variance across all samples and spatial locations as:

$$\mu_V = \frac{1}{S \cdot h \cdot w} \sum_{i=1}^S \sum_{x=1}^h \sum_{y=1}^w \mathbf{V}_i(x, y). \quad (15)$$

Here,  $\mu_V$  is a scalar value representing the global mean variance across all samples and pixels. By computing  $\mu_V$  for different diffusion steps, we observe that the global variance increases with the number of steps, as illustrated in Figure 3. Furthermore, we demonstrate that the variance control mechanism successfully aligns the global variance with that of CERRA-EDA, with the closest match achieved at  $N = 12$  diffusion steps.

## 5.2 Analyzing variance spatially

The global mean-variance inform us that the diffusion model is able to match the overall amount of variance present in CERRA-EDA, but this gives us no information to where the variance is distributed in space. Our interest here is to examine if there is a match between the two spatial distributions of the variance.

For the following experiments, we decided to investigate the variance in a three-monthly setting, to highlight the behavior of the model in different seasons. To achieve

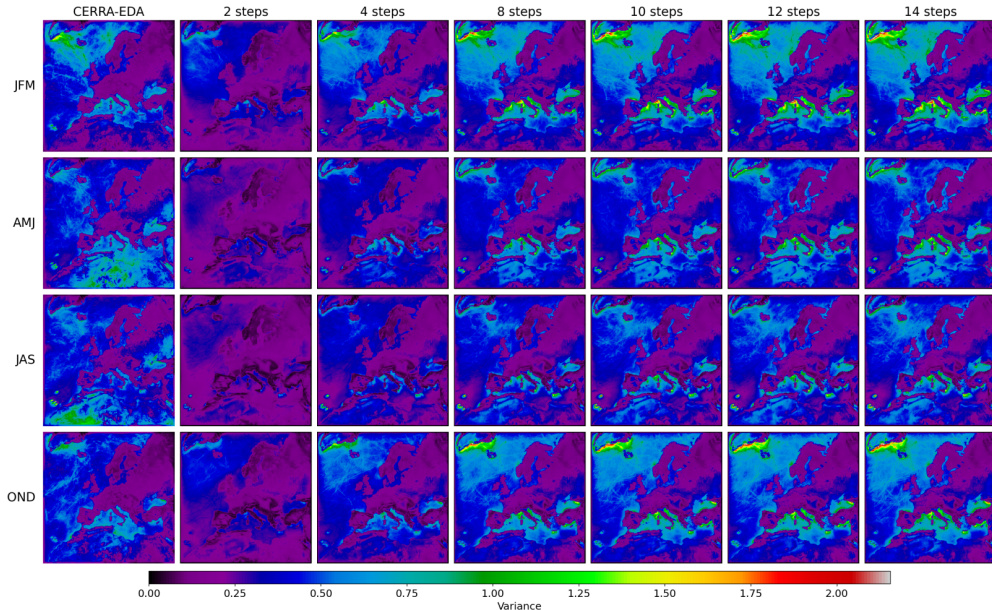


**Fig. 4:** Comparing the spatial variance of CERRA-EDA with ensemble diffusion at different diffusion steps. The comparison relative to the testing year 2016 and is performed in a 3 monthly manner to highlight seasonal variations.

this goal we divided the the samples into four sets, including respectively January February and March (JFM), April May and June (AMJ), July August and September (JAS) and October November and December (OND).

To analyze spatial variance, we compute the pixel-wise mean of variance maps across all samples within each three-monthly subset. Let  $k \in \{JFM, AMJ, JAS, OND\}$  denote the season,  $\mathcal{S}_k \subseteq \{1, \dots, S\}$  represent the subset of indices corresponding to the season  $k$ , and  $S_k$  the number of samples corresponding to season  $k$ . The spatial mean variance  $\mu_k^{spatial}$  for season  $k$  is given by:

$$\mu_k^{spatial}(x, y) = \frac{1}{S_k} \sum_{i \in \mathcal{S}_k} V_i(x, y), \quad (x, y) \in \{1, \dots, h\} \times \{1, \dots, w\}. \quad (16)$$

Here,  $V_i$  and  $\mu_k^{spatial}$  are understood to represent spatial fields, where the value of each pixel is computed independently. We compute the spatial mean-variance for the reference ensemble CERRA-EDA and for Ensemble Diffusion across a range of diffusion steps  $N \in \{2, 4, 8, 10, 12, 14\}$  for the year 2016. This allows us to visualize how the spatial distribution of variance evolves as the number of diffusion steps increases. The obtained results are reported in Figure 4. We observe substantial overlap between the variance distributions of CERRA-EDA and Ensemble Diffusion. This indicates that the diffusion model successfully captures the variability of the data by training solely on the CERRA dataset, without requiring additional information about the



underlying uncertainty. Furthermore, we note that the degree of spatial overlap varies by season, with the highest overlap observed in the JFM and OND sets, while AMJ and JAS exhibit less overlap.

To numerically quantify the overlap between variance distributions, we introduce the mean-variance discrepancy (MVD) score, a metric defined as the absolute error between the spatial mean-variance maps for each season. Let  $\boldsymbol{\mu}_{k,ED}^{\text{spatial}}$  denote the spatial mean-variance map of Ensemble Diffusion and  $\boldsymbol{\mu}_{k,CE}^{\text{spatial}}$  denote the corresponding map for CERRA-EDA. The MVD score for season  $k$  is then defined as:

$$\text{MVD}_k = \frac{1}{h \cdot w} \sum_{x=1}^h \sum_{y=1}^w \left| \boldsymbol{\mu}_{k,ED}^{\text{spatial}}(x, y) - \boldsymbol{\mu}_{k,CE}^{\text{spatial}}(x, y) \right|. \quad (17)$$

The numerical results for the MVD scores computed across all three-monthly periods are reported in Table 2.

From the MVD results, we observe that the optimal yearly number of diffusion steps is  $N = 8$ , a lower value if compared with 12, which was identified based on the global mean variance. This finding reveals that, while 12 steps yield an overall variance closest to the reference, the spatial distribution of the variance behaves differently. This underscores the importance of a tailored tuning procedure to achieve better alignment with expected uncertainties. Moreover, the MVD scores are not uniform throughout the year: the winter months achieve the lowest MVD scores with 4 diffusion steps, while the summer months perform best with 12 diffusion steps, possibly due to the model being affected by seasonal dynamics.

Alongside the full-domain analysis, we examine the behavior of the generated ensemble at a randomly selected point within the domain to provide a clearer and more readable visualization of the mean and variance ranges. For this analysis, we plot the mean value and variance range at the chosen point for both the 8-step ensemble diffusion and CERRA-EDA. To improve clarity over the high-frequency time series, we apply a moving average smoothing with a 30-sample window. The resulting plot, shown in Figure 5, reveals consistent overlap between the mean and variance ranges.

### 5.3 Impact of $\Delta t$ on performance

An interesting aspect of the variance analyses is to check how the overall performance of the Ensemble Diffusion (ED) model changes as the number of steps increase. To achieve this goal we have utilized  $M = 10$  ensemble members at  $565 \times 565$  spatial resolution and 6-hourly time resolution for the year 2016. We have computed the ensemble diffusion mean and compared it with the available CERRA-EDA control run, which is, as mentioned in Section 2.4, the member of the ensemble with no perturbation on the model input. We evaluate the comparison via MSE, calculated on normalized values. The results, reported in table 3, reveal that the performance is largely stable while changing the step size  $\Delta t$ , with a slight increase in the performance for larger step sizes. This should be expected as more steps allows the reverse diffusion process to make smaller, more gradual corrections at each step, leading to a more precise reconstruction of the target high-resolution image.

MVD Scores for Seasonal Spatial Variance Maps						
	2 steps	4 steps	8 steps	10 steps	12 steps	14 steps
<b>yearly</b>	1.18e-01	1.45e-01	<u>1.40e-01</u>	1.43e-01	1.45e-01	1.49e-01
<b>JFM</b>	1.14e-01	<u>1.02e-01</u>	1.10e-01	1.19e-01	1.27e-01	1.32e-01
<b>AMJ</b>	2.15e-01	1.62e-01	1.37e-01	1.34e-01	<u>1.33e-01</u>	1.34e-01
<b>JAS</b>	2.22e-01	1.74e-01	1.50e-01	1.47e-01	<u>1.46e-01</u>	1.47e-01
<b>OND</b>	1.42e-01	<u>1.10e-01</u>	1.17e-01	1.24e-01	<u>1.29e-01</u>	1.35e-01

**Table 2:** Mean variance discrepancy (MVD) scores computed between the spatial mean variance maps of Ensemble Diffusion and CERRA-EDA for each three-monthly period (JFM, AMJ, JAS, OND) and each timestamp for 2016. Lower scores indicate higher similarity between the variance distributions of the two ensembles.

MSE ensemble mean performance comparison						
	2 steps	4 steps	8 steps	10 steps	12 steps	14 steps
<b>JFM</b>	1.98e-03	1.92e-03	1.88e-03	1.87e-03	1.86e-03	<u>1.86e-03</u>
<b>AMJ</b>	1.52e-03	1.48e-03	1.46e-03	1.45e-03	1.45e-03	<u>1.44e-03</u>
<b>JAS</b>	1.39e-03	1.36e-03	1.33e-03	1.33e-03	1.33e-03	<u>1.32e-03</u>
<b>OND</b>	1.79e-03	1.73e-03	1.68e-03	1.68e-03	<u>1.67e-03</u>	<u>1.67e-03</u>

**Table 3:** Table comparing the MSE performance of the diffusion model at different numbers of reverse diffusion steps. The MSE is calculated between the mean of the 10 generated ensembles and the CERRA-EDA control run. The results are reported 3-monthly for the year 2016.

## 5.4 Demonstrating capabilities on CARRA

Both CERRA and CARRA, introduced in Section 2 are built upon the HARMONIE-AROME weather prediction system [50], adapted for reanalysis purposes. This common foundation ensures that both systems share a core methodology for atmospheric modeling and data assimilation, making them methodologically similar despite their focus on different regions.

Having validated our diffusion model’s capability to generate ensemble members for the CERRA dataset, we naturally extend this methodology to CARRA-EAST, the Arctic region dataset focusing on the eastern domain. Unlike CERRA, CARRA lacks an ensemble dataset, which limits its usability in quantifying variability, validating against real-world uncertainties, detecting rare or extreme events, performing ensemble-based statistical analyses, and estimating model robustness. Our ensemble diffusion driven ensemble dataset can be a highly efficient way to address this issues.

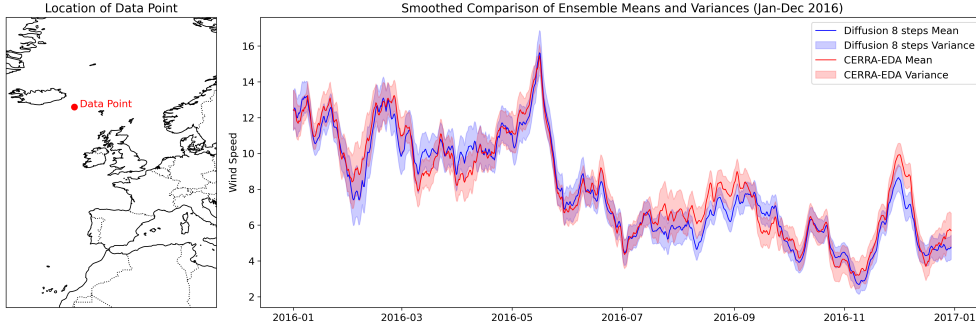


**Fig. 5:** Mean and variance range at a randomly selected point in the domain, compared between ensemble diffusion (8 reverse diffusion steps) and CERRA-EDA. Data is smoothed using a 30 samples moving average window for readability and covers the entire year of 2016.

For CARRA-EAST, we adopt a training setup similar to the one proposed for CERRA. The downscaling process is framed as an image-to-image transformation, converting low-resolution ERA5 data into high-resolution CARRA-EAST, maintaining the same spatial domain between the two, with the resulting grid having a size of  $989 \times 789$ . We regrid ERA5 wind speed data to match the projection of CARRA-EAST. The training period spans 1991–2010, while the year 2016 is reserved for ensemble testing. As with CERRA, padding is applied to adjust the grid size for compatibility with the diffusion architecture. Training was conducted following the setup detailed in Section 4.2.

The ensemble members are generated for the year 2016 using 8 diffusion steps, the optimal value determined through spatial validation with MVD on CERRA-EDA. Figure 6 illustrates the spatial variance for 2016, plotted within the same variance range as Figure 4. Our results reveal that the spatial variance is consistent with expected patterns.

## 6 Conclusions

In this work, we applied an ensemble diffusion model to the full-domain ERA5-to-CERRA downscaling task and discovered a relationship between the variance exhibited by the ensemble diffusion and the number of reverse diffusion steps, giving theoretical proof of this relation. Notably, we demonstrated that the selection of the reverse diffusion step size  $\Delta t$  not only impacts the time efficiency of the generative process but also serves as a crucial mechanism for controlling the variance of the sampled data, a key aspect when using these models for generating ensembles. We have explored architectural improvements needed to apply ensemble diffusion models over large domains, including the use of a scaling factor to reduce the signal rate in the noise scheduler, reducing the effect that higher resolution have on denoising difficulty. Our experimental results indicate that adjusting the number of diffusion steps enables the model to operate across different ranges of ensemble variance. We found that the

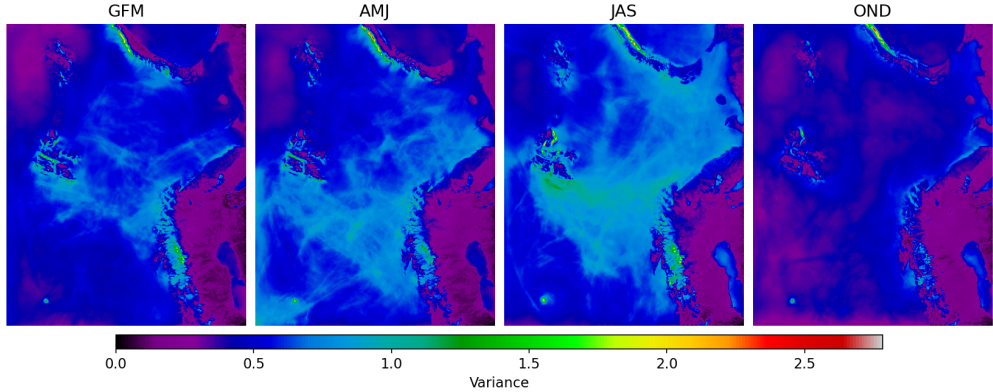


**Fig. 6:** Revealing the spatial variance of ensemble diffusion trained on CARRA-EAST with 8 diffusion steps. The comparison is relative to the testing year 2016 and is performed in a 3 monthly manner to highlight seasonal variations.

control over variance gained by varying the number of diffusion steps is sufficient to match the global mean variance exhibited by the available ensemble reference dataset, CERRA-EDA. We observed that increasing the number of diffusion steps leads to convergence toward a fixed variance value. Although this converged global mean variance closely matches the one exhibited by CERRA-EDA, our MVD score, which takes into account the spatial distribution of the variance, revealed that the optimal number of steps is 8, a value far from the convergence point. This demonstrates that selecting a “sufficiently high” number of steps is not necessarily an optimal strategy for tuning an ensemble diffusion model, highlighting the importance of calibration to obtain optimal results. Interestingly, the relationship between the number of steps and ensemble variance may have been overlooked in previous research, as it is common practice to run diffusion models with a high number of steps [28, 31, 51]. In such cases, the overall variance would have already converged to a fixed value, making it unaffected by changes in the number of reverse diffusion steps. In our work we have showcased the capability of generating ensemble members efficiently at high temporal and spatial resolutions. Specifically, our ensemble reference CERRA-EDA has a considerable reduction in spatial resolution (from  $1069 \times 1069$  to  $565 \times 565$ ) and temporal resolution (from  $3h$  to  $6h$ ). We reveal that our approach is able to generate ensemble members at full CERRA temporal and spatial resolution, while maintaining high efficiency, essentially running on workstation hardware. Considering that our model is conditioned only by ERA5 low-resolution inputs, which happens to be available at hourly intervals, we can additionally increase the ensemble temporal resolution to  $1h$ . Additionally, we have extended our ensemble diffusion methodology from CERRA to CARRA-EAST, demonstrating its capability to generate ensemble members for datasets lacking ensemble information, using a similar training setup and confirming its effectiveness in reproducing spatial variance patterns through diffusion step tuning.

Since our diffusion model is trained solely on the deterministic ERA5-to-CERRA task, it is unaffected by factors such as measurement quality or other previously

assessed uncertainties. As such, our approach can serve as a validation tool for existing ensembles, with discrepancies providing insights into the neural model’s understanding of the underlying physical system or serving as validation for uncertainty estimates obtained through other methods. In our experimental setting, the spatial variance reported in Figure 4 shows a clear overlap between distributions. However, during the summer months in the North African region, discrepancies between CERRA-EDA and our Ensemble Diffusion appear. This may indicate that our model struggles to capture uncertainty in this region, or that CERRA-EDA itself may be affected by data scarcity [6].

In conclusion, our methodology provides a practical tool for tuning ensemble diffusion models to produce the correct variance distribution. We anticipate that future implementations will consider the number of diffusion steps as a crucial tuning parameter. Furthermore, our theoretical framework opens promising directions for studying the statistical properties of ensemble members in relation to the structure of diffusion models, encouraging further research.

## 7 Acknowledgements

ERA5, CERRA, CERRA-EDA and CARRA were downloaded from the Copernicus Climate Change Service (C3S) (2023). This research was partially funded and supported by the following Projects:

- European Cordis Project “Optimal High Resolution Earth System Models for Exploring Future Climate Changes” (OptimESM), Grant agreement ID: 101081193
- IS CRA Project “AI for weather analysis and forecast” (AIWAF)

## Statements and Declarations

The authors declare no competing interests.

## Code availability

The code and downscaled ensemble members relative to the presented work is archived at the following GitHub <https://github.com/fmerizzi/ERA5-to-CERRA-via-Diffusion-Models/>. We also provide the full list of the environmental libraries and respective versions.

## References

- [1] Olaf Ronneberger, Philipp Fischer, and Thomas Brox. U-net: Convolutional networks for biomedical image segmentation, 2015.
- [2] Ze Liu, Yutong Lin, Yue Cao, Han Hu, Yixuan Wei, Zheng Zhang, Stephen Lin, and Baining Guo. Swin transformer: Hierarchical vision transformer using shifted windows. In *Proceedings of the IEEE/CVF international conference on computer vision*, pages 10012–10022, 2021.
- [3] Jonathan Ho, Ajay Jain, and Pieter Abbeel. Denoising diffusion probabilistic models. *Advances in neural information processing systems*, 33:6840–6851, 2020.

- [4] Jiaming Song, Chenlin Meng, and Stefano Ermon. Denoising diffusion implicit models, 2022.
- [5] H. Hersbach, B. Bell, P. Berrisford, G. Biavati, A. Horányi, J. Muñoz Sabater, J. Nicolas, C. Peubey, R. Radu, I. Rozum, D. Schepers, A. Simmons, C. Soci, D. Dee, and J-N. Thépaut. ERA5 hourly data on single levels from 1940 to present. *Copernicus Climate Change Service (C3S) Climate Data Store (CDS)*, 2018. Accessed on 22-11-2023.
- [6] Martin Ridal, Eric Bazile, Patrick Le Moigne, Roger Randriamampianina, Semjon Schimanke, Ulf Andrae, Lars Berggren, Pierre Brousseau, Per Dahlgren, Lisette Edvinsson, et al. Cerra, the copernicus european regional reanalysis system. *Quarterly Journal of the Royal Meteorological Society*, 2024.
- [7] Fabio Merizzi, Andrea Asperti, and Stefano Colamonaco. Wind speed super-resolution and validation: from era5 to cerra via diffusion models. *Neural Computing and Applications*, Sep 2024.
- [8] Copernicus Climate Change Service. Copernicus arctic regional reanalysis service, 2024. Accessed: 2024-12-11.
- [9] Hao Sun, Baichi Zhou, Chuanjun Zhang, Hongxing Liu, and Bo Yang. Dscale\_mod16: A model for disaggregating microwave satellite soil moisture with land surface evapotranspiration products and gridded meteorological data. *Remote Sensing*, 12(6), 2020.
- [10] Andreise Moreira, Denise Cybis Fontana, and Tatiana Mora Kuplich. Wavelet approach applied to evi/modis time series and meteorological data. *ISPRS Journal of Photogrammetry and Remote Sensing*, 147:335–344, 2019.
- [11] Harald Zandler, Thomas Senftl, and Kim André Vanselow. Reanalysis datasets outperform other gridded climate products in vegetation change analysis in peripheral conservation areas of central asia. *Scientific Reports*, 10(1):22446, 2020.
- [12] David W. Pierce, Tim P. Barnett, Benjamin D. Santer, and Peter J. Gleckler. Selecting global climate models for regional climate change studies. *Proceedings of the National Academy of Sciences*, 106(21):8441–8446, 2009.
- [13] Naomi Goldenson, L. Ruby Leung, Linda O. Mearns, David W. Pierce, Kevin A. Reed, Isla R. Simpson, Paul Ullrich, Will Krantz, Alex Hall, Andrew Jones, and Stefan Rahimi. Use-inspired, process-oriented gcm selection: Prioritizing models for regional dynamical downscaling. *Bulletin of the American Meteorological Society*, 104(9):E1619 – E1629, 2023.
- [14] Yongjian Sun, Kefeng Deng, Kaijun Ren, Jia Liu, Chongjiu Deng, and Yongjun Jin. Deep learning in statistical downscaling for deriving high spatial resolution gridded meteorological data: A systematic review, 2 2024.
- [15] Antonio Pérez, Mario Santa Cruz, Daniel San Martín, and José Manuel Gutiérrez. Transformer based super-resolution downscaling for regional reanalysis: Full domain vs tiling approaches. *arXiv preprint arXiv:2410.12728*, 2024.
- [16] Thomas Vandal, Evan Kodra, Sangram Ganguly, Andrew Michaelis, Ramakrishna Nemani, and Auroop R Ganguly. Deepisd: Generating high resolution climate change projections through single image super-resolution, 2017.

- [17] Jianxin Cheng, Jin Liu, Qiuming Kuang, Zhou Xu, Chenkai Shen, Wang Liu, and Kang Zhou. Deepdt: Generative adversarial network for high-resolution climate prediction. *IEEE Geoscience and Remote Sensing Letters*, 19:1–5, 2022.
- [18] Jia Liu, Yongjian Sun, Kaijun Ren, Yanlai Zhao, Kefeng Deng, and Lizhe Wang. A spatial downscaling approach for windsat satellite sea surface wind based on generative adversarial networks and dual learning scheme. *Remote Sensing*, 14(3), 2022.
- [19] Yan Ji, Xiefei Zhi, Ye Tian, Ting Peng, Ziqiang Huo, and Luying Ji. Downscaling of precipitation forecasts based on single image super-resolution. In *EGU General Assembly Conference Abstracts*, page 8533, 2020.
- [20] Lucy Harris, Andrew T. T. McRae, Matthew Chantry, Peter D. Dueben, and Tim N. Palmer. A generative deep learning approach to stochastic downscaling of precipitation forecasts. *Journal of Advances in Modeling Earth Systems*, 14(10):e2022MS003120, 2022. e2022MS003120 2022MS003120.
- [21] Linsey S Passarella, Salil Mahajan, Anikesh Pal, and Matthew R Norman. Reconstructing high resolution esm data through a novel fast super resolution convolutional neural network (fsrncn). *Geophysical Research Letters*, 49(4):e2021GL097571, 2022.
- [22] Dánnell Quesada-Chacón, Klemens Barfus, and Christian Bernhofer. Repeatable high-resolution statistical downscaling through deep learning. *Geoscientific Model Development*, 15(19):7353–7370, 2022.
- [23] Shuangyi Zhang and Xichen Li. Future projections of offshore wind energy resources in china using cmip6 simulations and a deep learning-based downscaling method. *Energy*, 217:119321, 2021.
- [24] Tung Nguyen, Jason Jewik, Hritik Bansal, Prakhar Sharma, and Aditya Grover. Climatelearn: Benchmarking machine learning for weather and climate modeling. *arXiv preprint arXiv:2307.01909*, 2023.
- [25] P. Harder, Qidong Yang, Venkatesh Ramesh, P. Sattigeri, Alex Hernández-García, C. Watson, D. Szwarcman, and D. Rolnick. Generating physically-consistent high-resolution climate data with hard-constrained neural networks. *ArXiv*, abs/2208.05424, 2022.
- [26] Jérôme Dujardin and Michael Lehning. Wind-topo: Downscaling near-surface wind fields to high-resolution topography in highly complex terrain with deep learning. *Quarterly Journal of the Royal Meteorological Society*, 148(744):1368–1388, 2022.
- [27] Tingzhao Yu, Ruyi Yang, Yan Huang, Jinbing Gao, and Qiuming Kuang. Terrain-guided flatten memory network for deep spatial wind downscaling. *IEEE Journal of Selected Topics in Applied Earth Observations and Remote Sensing*, 15:9468–9481, 2022.
- [28] Ilan Price, Alvaro Sanchez-Gonzalez, Ferran Alet, Tom R Andersson, Andrew El-Kadi, Dominic Masters, Timo Ewalds, Jacklynn Stott, Shakir Mohamed, Peter Battaglia, et al. Gencast: Diffusion-based ensemble forecasting for medium-range weather. *arXiv preprint arXiv:2312.15796*, 2023.
- [29] Morteza Mardani, Noah Brenowitz, Yair Cohen, Jaideep Pathak, Chieh-Yu Chen, Cheng-Chin Liu, Arash Vahdat, Mohammad Amin Nabian, Tao Ge, Akshay

- Subramaniam, Karthik Kashinath, Jan Kautz, and Mike Pritchard. Residual corrective diffusion modeling for km-scale atmospheric downscaling, 2024.
- [30] Ignacio Lopez-Gomez, Zhong Yi Wan, Leonardo Zepeda-Núñez, Tapio Schneider, John Anderson, and Fei Sha. Dynamical-generative downscaling of climate model ensembles, 2024.
- [31] Fenghua Ling, Zeyu Lu, Jing-Jia Luo, Lei Bai, Swadhin K Behera, Dachao Jin, Baoxiang Pan, Huidong Jiang, and Toshio Yamagata. Diffusion model-based probabilistic downscaling for 180-year east asian climate reconstruction. *npj Climate and Atmospheric Science*, 7(1):131, 2024.
- [32] Lizao Li, Robert Carver, Ignacio Lopez-Gomez, Fei Sha, and John Anderson. Generative emulation of weather forecast ensembles with diffusion models. *Science Advances*, 10(13):eadk4489, 2024.
- [33] Zhong Yi Wan, Ricardo Baptista, Anudhyan Boral, Yi-Fan Chen, John Anderson, Fei Sha, and Leonardo Zepeda-Núñez. Debias coarsely, sample conditionally: Statistical downscaling through optimal transport and probabilistic diffusion models. *Advances in Neural Information Processing Systems*, 36:47749–47763, 2023.
- [34] Andrea Asperti, Fabio Merizzi, Alberto Paparella, Giorgio Pedrazzi, Matteo Angelinelli, and Stefano Colamonaco. Precipitation nowcasting with generative diffusion models. *arXiv preprint arXiv:2308.06733*, 2023.
- [35] Jussi Leinonen, Ulrich Hamann, Daniele Nerini, Urs Germann, and Gabriele Franch. Latent diffusion models for generative precipitation nowcasting with accurate uncertainty quantification. *arXiv preprint arXiv:2304.12891*, 2023.
- [36] A. Wootten, E. Massoud, A. Sengupta, D. Waliser, and Huikyo Lee. The effect of statistical downscaling on the weighting of multi-model ensembles of precipitation. *Climate*, 2020.
- [37] Ignacio Lopez-Gomez, Zhong Yi Wan, Leonardo Zepeda-Núñez, Tapio Schneider, John Anderson, and Fei Sha. Dynamical-generative downscaling of climate model ensembles. *arXiv preprint arXiv:2410.01776*, 2024.
- [38] Joseph W. Lockwood, Avantika Gori, and Pierre Gentine. A generative super-resolution model for enhancing tropical cyclone wind field intensity and resolution. *Journal of Geophysical Research: Machine Learning and Computation*, 1, 12 2024.
- [39] Kevin E Trenberth, John T Fasullo, and Theodore G Shepherd. Attribution of climate extreme events. *Nature climate change*, 5(8):725–730, 2015.
- [40] Kai Kornhuber, Corey Lesk, Carl Schleussner, Jonas Jägermeyr, Peter Pfleiderer, and Radley Horton. Risks of synchronized low yields are underestimated in climate and crop model projections. *Nature Communications*, 14, 07 2023.
- [41] W. B. Anderson, R. Seager, W. Baethgen, M. Cane, and L. You. Synchronous crop failures and climate-forced production variability. *Science Advances*, 5(7):eaaw1976, 2019.
- [42] Andrea Asperti, Davide Evangelista, Samuele Marro, and Fabio Merizzi. Image embedding for denoising generative models. *Artificial Intelligence Review*, 56(12):14511–14533, 2023.
- [43] Tero Karras, Miika Aittala, Timo Aila, and Samuli Laine. Elucidating the design space of diffusion-based generative models. *Advances in neural information*



- processing systems*, 35:26565–26577, 2022.
- [44] Hans Hersbach, Bill Bell, Paul Berrisford, Shoji Hirahara, András Horányi, Joaquín Muñoz-Sabater, Julien Nicolas, Carole Peubey, Raluca Radu, Dinand Schepers, et al. The era5 global reanalysis. *Quarterly Journal of the Royal Meteorological Society*, 146(730):1999–2049, 2020.
- [45] Martin Ridal, Eric Bazile, Patrick Le Moigne, Roger Randriamampianina, Semjon Schimanke, Ulf Andrae, Lars Berggren, Pierre Brousseau, Per Dahlgren, Lisette Edvinsson, Adam El-Said, Michael Glinton, Susanna Hagelin, Susanna Hopsch, Ludvig Isaksson, Paulo Medeiros, Esbjörn Olsson, Per Unden, and Zheng Qi Wang. Cerra, the copernicus european regional reanalysis system. *Quarterly Journal of the Royal Meteorological Society*, 2024.
- [46] Alexander Quinn Nichol and Prafulla Dhariwal. Improved denoising diffusion probabilistic models. In *International conference on machine learning*, pages 8162–8171. PMLR, 2021.
- [47] Ting Chen. On the importance of noise scheduling for diffusion models. *arXiv preprint arXiv:2301.10972*, 2023.
- [48] Emiel Hoogeboom, Jonathan Heek, and Tim Salimans. simple diffusion: End-to-end diffusion for high resolution images. In *International Conference on Machine Learning*, pages 13213–13232. PMLR, 2023.
- [49] Kaiming He, Xiangyu Zhang, Shaoqing Ren, and Jian Sun. Deep residual learning for image recognition. In *2016 IEEE Conference on Computer Vision and Pattern Recognition (CVPR)*, pages 770–778, 2016.
- [50] Lisa Bengtsson, Ulf Andrae, Trygve Aspelién, Yurii Batrak, Javier Calvo, Wim de Rooy, Emily Gleeson, Bent Hansen-Sass, Mariken Homleid, Mariano Hortal, et al. The harmonie–arome model configuration in the aladin–hirlam nwp system. *Monthly Weather Review*, 145(5):1919–1935, 2017.
- [51] Seth Bassetti, Brian Hutchinson, Claudia Tebaldi, and Ben Kravitz. Diffesm: Conditional emulation of temperature and precipitation in earth system models with 3d diffusion models. *Journal of Advances in Modeling Earth Systems*, 16(10):e2023MS004194, 2024.

## A Proofs of main results

In this section, we report the derivation of the main results presented in the paper.

### A.1 Properties of element-wise variance

At first, we need to show that element-wise variance  $\mathbf{v}(\mathbf{x}_t)$ , defined in (10) inherits similar properties as the full variance, and in particular (P1) and (P2). This is not hard to prove, as:

$$\mathbf{v}(a\mathbf{x}_t)_i = \text{Var}(a\mathbf{x}_t)_{i,i} = a^2 \text{Var}(\mathbf{x}_t)_{i,i} = a^2 \mathbf{v}(\mathbf{x}_t)_i,$$

and:

$$\mathbf{v}(\mathbf{x}_t + \mathbf{y}_t)_i = \text{Var}(\mathbf{x}_t + \mathbf{y}_t)_{i,i} = \text{Var}(\mathbf{x}_t)_{i,i} + \text{Var}(\mathbf{y}_t)_{i,i} + 2\text{Cov}(\mathbf{x}_t, \mathbf{y}_t)_{i,i}$$

$$= \mathbf{v}(\mathbf{x}_t)_i + \mathbf{v}(\mathbf{y}_t)_i + 2\mathbf{v}(\mathbf{x}_t, \mathbf{y}_t)_i,$$

which proves the required properties.

## A.2 Proof of Proposition 3.1

The essence of our theoretical results lies on the recursive formula introduced in Proposition 3.1, which follows by properties (P1) and (P2) applied to the diffusion process (4). In particular note that, by (4),

$$\mathbf{v}(\mathbf{x}_t) = \mathbf{v} \left( \frac{\alpha_t}{\alpha_{t-\Delta t}} \mathbf{x}_{t-\Delta t} + c_{t-\Delta t} \boldsymbol{\epsilon}_{\Theta}^{t-\Delta t}(\mathbf{x}_{t-\Delta t}) \right).$$

Then, applying (P1) and (P2),

$$\begin{aligned} \mathbf{v}(\mathbf{x}_t) &= \frac{\alpha_t}{\alpha_{t-\Delta t}} \mathbf{v}(\mathbf{x}_{t-\Delta t}) + c_{t-\Delta t}^2 \mathbf{v}(\boldsymbol{\epsilon}_{\Theta}^{t-\Delta t}(\mathbf{x}_{t-\Delta t})) \\ &\quad + 2\sqrt{\frac{\alpha_t}{\alpha_{t-\Delta t}}} c_{t-\Delta t} \mathbf{v}(\mathbf{x}_{t-\Delta t}, \boldsymbol{\epsilon}_{\Theta}^{t-\Delta t}(\mathbf{x}_{t-\Delta t})). \end{aligned}$$

Since by (2),  $\boldsymbol{\epsilon}_{\Theta}^{t-\Delta t}(\mathbf{x}_{t-\Delta t}) \approx \boldsymbol{\epsilon}_{t-\Delta t}$ , then  $\mathbf{v}(\boldsymbol{\epsilon}_{\Theta}^{t-\Delta t}(\mathbf{x}_{t-\Delta t})) \approx \mathbf{v}(\boldsymbol{\epsilon}_{t-\Delta t}) = \mathbf{1}$ , which results in:

$$\mathbf{v}(\mathbf{x}_t) = \frac{\alpha_t}{\alpha_{t-\Delta t}} \mathbf{v}(\mathbf{x}_{t-\Delta t}) + c_{t-\Delta t}^2 \mathbf{1} + 2\sqrt{\frac{\alpha_t}{\alpha_{t-\Delta t}}} c_{t-\Delta t} \mathbf{v}(\mathbf{x}_{t-\Delta t}, \boldsymbol{\epsilon}_{\Theta}^{t-\Delta t}(\mathbf{x}_{t-\Delta t})).$$

To simplify this expression, recall the definition of the covariance:

$$\mathbf{v}(\mathbf{x}_{t-\Delta t}, \boldsymbol{\epsilon}_{\Theta}^{t-\Delta t}(\mathbf{x}_{t-\Delta t})) = \mathbb{E} \left[ (\mathbf{x}_{t-\Delta t} - \mathbf{m}_{t-\Delta t})(\boldsymbol{\epsilon}_{\Theta}^{t-\Delta t}(\mathbf{x}_{t-\Delta t}) - \mathbb{E}[\boldsymbol{\epsilon}_{\Theta}^{t-\Delta t}(\mathbf{x}_{t-\Delta t})])^T \right],$$

where we denoted  $\mathbf{m}_{t-\Delta t} := \mathbb{E}[\mathbf{x}_{t-\Delta t}]$ , and consider the first order Taylor decomposition of  $\boldsymbol{\epsilon}_{\Theta}^{t-\Delta t}(\mathbf{x}_{t-\Delta t})$  around  $\mathbf{m}_{t-\Delta t}$ :

$$\boldsymbol{\epsilon}_{\Theta}^{t-\Delta t}(\mathbf{x}_{t-\Delta t}) \approx \boldsymbol{\epsilon}_{\Theta}^{t-\Delta t}(\mathbf{m}_{t-\Delta t}) + \nabla_{\mathbf{m}_{t-\Delta t}} \boldsymbol{\epsilon}_{\Theta}^{t-\Delta t}(\mathbf{m}_{t-\Delta t})(\mathbf{x}_{t-\Delta t} - \mathbf{m}_{t-\Delta t}).$$

Consequently:

$$\begin{aligned} \mathbb{E}[\boldsymbol{\epsilon}_{\Theta}^{t-\Delta t}(\mathbf{x}_{t-\Delta t})] &\approx \mathbb{E}[\boldsymbol{\epsilon}_{\Theta}^{t-\Delta t}(\mathbf{m}_{t-\Delta t}) + \nabla_{\mathbf{m}_{t-\Delta t}} \boldsymbol{\epsilon}_{\Theta}^{t-\Delta t}(\mathbf{m}_{t-\Delta t})(\mathbf{x}_{t-\Delta t} - \mathbf{m}_{t-\Delta t})] \\ &= \boldsymbol{\epsilon}_{\Theta}^{t-\Delta t}(\mathbf{m}_{t-\Delta t}) + \nabla_{\mathbf{m}_{t-\Delta t}} \boldsymbol{\epsilon}_{\Theta}^{t-\Delta t}(\mathbf{m}_{t-\Delta t}) \mathbb{E}[(\mathbf{x}_{t-\Delta t} - \mathbf{m}_{t-\Delta t})] \\ &= \boldsymbol{\epsilon}_{\Theta}^{t-\Delta t}(\mathbf{m}_{t-\Delta t}), \end{aligned}$$

where in the first equality we used the linearity of the expected value and the observation that  $\mathbb{E}[\boldsymbol{\epsilon}_{\Theta}^{t-\Delta t}(\mathbf{m}_{t-\Delta t})] = \boldsymbol{\epsilon}_{\Theta}^{t-\Delta t}(\mathbf{m}_{t-\Delta t})$  as  $\boldsymbol{\epsilon}_{\Theta}^{t-\Delta t}(\mathbf{m}_{t-\Delta t})$  is constant with respect to  $\mathbf{x}_{t-\Delta t}$ , while the second equality follows by observing that:

$$\mathbb{E}[(\mathbf{x}_{t-\Delta t} - \mathbf{m}_{t-\Delta t})] = \mathbb{E}[\mathbf{x}_{t-\Delta t}] - \mathbb{E}[\mathbf{m}_{t-\Delta t}] = \mathbf{m}_{t-\Delta t} - \mathbf{m}_{t-\Delta t} = \mathbf{0}.$$

Plugging the equations above into the definition of covariance, we get:

$$\begin{aligned}
\mathbf{v}(\mathbf{x}_{t-\Delta t}, \boldsymbol{\epsilon}_{\Theta}^{t-\Delta t}(\mathbf{x}_{t-\Delta t})) &\approx \mathbb{E} \left[ (\mathbf{x}_{t-\Delta t} - \mathbf{m}_{t-\Delta t})(\boldsymbol{\epsilon}_{\Theta}^{t-\Delta t}(\mathbf{x}_{t-\Delta t}) - \boldsymbol{\epsilon}_{\Theta}^{t-\Delta t}(\mathbf{m}_{t-\Delta t}))^T \right] \\
&\approx \mathbb{E} \left[ (\mathbf{x}_{t-\Delta t} - \mathbf{m}_{t-\Delta t})(\nabla_{\mathbf{m}_{t-\Delta t}} \boldsymbol{\epsilon}_{\Theta}^{t-\Delta t}(\mathbf{m}_{t-\Delta t})(\mathbf{x}_{t-\Delta t} - \mathbf{m}_{t-\Delta t}))^T \right] \\
&= \nabla_{\mathbf{m}_{t-\Delta t}} \boldsymbol{\epsilon}_{\Theta}^{t-\Delta t}(\mathbf{m}_{t-\Delta t}) \mathbb{E} \left[ (\mathbf{x}_{t-\Delta t} - \mathbf{m}_{t-\Delta t})(\mathbf{x}_{t-\Delta t} - \mathbf{m}_{t-\Delta t})^T \right] \\
&= \nabla_{\mathbf{m}_{t-\Delta t}} \boldsymbol{\epsilon}_{\Theta}^{t-\Delta t}(\mathbf{m}_{t-\Delta t}) \mathbf{v}(\mathbf{x}_{t-\Delta t}).
\end{aligned}$$

Substituting this result back into the equation for the variance of  $\mathbf{x}_t$ , we get:

$$\begin{aligned}
\mathbf{v}(\mathbf{x}_t) &= \frac{\alpha_t}{\alpha_{t-\Delta t}} \mathbf{v}(\mathbf{x}_{t-\Delta t}) + c_{t-\Delta t}^2 \mathbf{1} + 2 \sqrt{\frac{\alpha_t}{\alpha_{t-\Delta t}}} c_{t-\Delta t} \nabla_{\mathbf{m}_{t-\Delta t}} \boldsymbol{\epsilon}_{\Theta}^{t-\Delta t}(\mathbf{m}_{t-\Delta t}) \mathbf{v}(\mathbf{x}_{t-\Delta t}) \\
&= \left( \frac{\alpha_t}{\alpha_{t-\Delta t}} \mathbf{1} + 2 \sqrt{\frac{\alpha_t}{\alpha_{t-\Delta t}}} c_{t-\Delta t} \nabla_{\mathbf{m}_{t-\Delta t}} \boldsymbol{\epsilon}_{\Theta}^{t-\Delta t}(\mathbf{m}_{t-\Delta t}) \right) \mathbf{v}(\mathbf{x}_{t-\Delta t}) + c_{t-\Delta t}^2 \mathbf{1},
\end{aligned}$$

which corresponds to Proposition 3.1 by setting:

$$\begin{aligned}
\mathbf{F}_t &:= \frac{\alpha_t}{\alpha_{t-\Delta t}} \mathbf{1} + 2 \sqrt{\frac{\alpha_t}{\alpha_{t-\Delta t}}} c_{t-\Delta t} \nabla_{\mathbf{m}_{t-\Delta t}} \boldsymbol{\epsilon}_{\Theta}^{t-\Delta t}(\mathbf{m}_{t-\Delta t}), \\
\mathbf{g}_t &:= c_{t-\Delta t}^2 \mathbf{1}.
\end{aligned}$$

### A.3 Proof of Theorem 3.2

The proof of the next Theorem is mainly a recursive application of Proposition 3.1 to compute  $\mathbf{v}_T$  from  $\mathbf{v}_0$ . Indeed, we recall that:

$$\mathbf{v}_t \approx \mathbf{F}_t \mathbf{v}_{t-\Delta t} + \mathbf{g}_t.$$

Since, as already observed,  $\mathbf{v}_0 = \mathbf{1}$ , then:

$$\begin{aligned}
\mathbf{v}_{\Delta t} &\approx \mathbf{F}_{\Delta t} \mathbf{1} + \mathbf{g}_{\Delta t}, \\
\mathbf{v}_{2\Delta t} &\approx \mathbf{F}_{2\Delta t} \mathbf{F}_{\Delta t} \mathbf{1} + \mathbf{F}_{2\Delta t} \mathbf{g}_{\Delta t} + \mathbf{g}_{2\Delta t}, \\
\mathbf{v}_{3\Delta t} &\approx \mathbf{F}_{3\Delta t} \mathbf{F}_{2\Delta t} \mathbf{F}_{\Delta t} \mathbf{1} + \mathbf{F}_{3\Delta t} \mathbf{F}_{2\Delta t} \mathbf{g}_{\Delta t} + \mathbf{F}_{3\Delta t} \mathbf{g}_{2\Delta t} + \mathbf{g}_{3\Delta t}, \\
&\dots \\
\mathbf{v}_{N\Delta t} &\approx \left( \prod_{i=1}^N \mathbf{F}_{i\Delta t} \right) \mathbf{1} + \sum_{i=1}^N \left( \prod_{k=i+1}^{N+1} \mathbf{F}_{k\Delta t} \right) \mathbf{g}_{i\Delta t},
\end{aligned}$$

where we defined  $\mathbf{F}_{(N+1)\Delta t} := \mathbf{I}$  for simplicity, concluding the proof.